Chinese Chemical Letters 31 (2020) 1226–1230

Contents lists available at ScienceDirect

Chinese Chemical Letters

journal homepage: www.elsevier.com/locate/cclet

Communication

Highly active N, O-doped hierarchical porous carbons for high-energy supercapacitors

Ziyang Zhou[a,1], Ling Miao[a,1], Hui Duan[a], Zhiwei Wang[b], Yaokang Lv[c], Wei Xiong[e], Dazhang Zhu[a], Liangchun Li[a], Mingxian Liu[a,b,d,**], Lihua Gan[a,*]

[a] Shanghai Key Lab. of Chemical Assessment and Sustainability, School of Chemical Science and Engineering, Tongji University, Shanghai 200092, China
[b] State Key Laboratory of Pollution Control and Resources Reuse, Shanghai Institute of Pollution Control and Ecological Security, School of Environmental Science and Engineering, Tongji University, Shanghai 200092, China
[c] College of Chemical Engineering, Zhejiang University of Technology, Hangzhou 310014, China
[d] College of Chemistry and Molecular Engineering, Zhengzhou University, Zhengzhou 450001, China
[e] School of Chemistry and Environmental Engineering, Key Laboratory for Green Chemical Process (Ministry of Education), Hubei Key Lab. of Novel Reactor & Green Chemical Technology, Wuhan Institute of Technology, Wuhan 430205, China

ARTICLE INFO

Article history:
Received 6 January 2020
Received in revised form 4 February 2020
Accepted 13 February 2020
Available online 14 February 2020

Keywords:
N, O-doped carbon
Hierarchical porous structure
Faradaic activity
Supercapacitor
High energy density

ABSTRACT

Highly active N, O-doped hierarchical porous carbons (NOCs) are fabricated through the *in-situ* polymerization and pyrolysis of *o*-tolidine and *p*-benzoquinone. As-prepared NOCs have a variety of faradaic-active species (N-6, N-5 and O-I), high ion-accessible platform (1799 m^2/g) and hierarchically micro–meso–macro porous architecture. Consequently, the resultant NOC electrode delivers an advantageous specific capacitance (311 F/g), with a pseudocapacitive contribution of 37% in a three-electrode configuration, and an enhanced energy output of 18.0 Wh/kg @ 350 W/kg owing to the enlarged faradaic effect in an aqueous redox-active cell. Besides, a competitive energy density (74.9 Wh/kg) and high-potential durability (87.8%) are achieved in an ionic liquid ($EMIMBF_4$)-assembled device. This study sheds light on a straightforward avenue to optimize the faradaic activity and nanoarchitecture for advanced supercapacitors.

Climatic deterioration and energy crisis have aroused global concern in searching for sustainable energy-storage apparatuses [1–3]. Supercapacitors stand out by virtue of the advantageous power density and cycle stability [4–6]. However, boosting the energy storage without sacrificing power/cycling performance is fundamental for their practical applications [7]. Generally, supercapacitors are divided into electric double-layer capacitors based on a physical charge-storage mechanism, and pseudo-capacitors relying on transition metal oxides and conducting polymers with redox activities [8,9]. Since the former way is purely electrostatic, the capacitance is positively correlated with the quantity of electrolyte ions stored on the electrode surface, and thus large surface area is essential [10,11]. While the latter delivers pseudocapacitance realized by rapid faradaic reactions, but the long-term stability and power density would be compromised [12–14].

Heteroatom-doped carbon supercapacitors integrate both large adsorbing carbon surfaces and faradaic-active heteroatom species [15,16]. A high ion-accessible carbon surface is the prerequisite for sufficient electrostatic adsorption sites [17,18]. For one thing, hierarchical pore distribution is responsible for effective utilization of the surface area to maximize adsorbed ions on electrode materials [11,19]. This is because micropores contribute to the formation of electric double layers, and larger pores serve as highways to cut down the distance from internal surface to interface [20,21]. For another, doping heteroatoms (N, P, O, S, *etc.*) into carbon matrix can break the electroneutrality of neighbored C atoms, thus modifying surface polarization/affinity toward electrolyte for enhanced electrostatic interaction [22–24]. More importantly, faradaic-active species (*e.g.*, pyrrolic N, pyridinic N and quinone O) also yield the pseudocapacitance through redox reactions [25,26]. Nevertheless, overmuch incorporation of heteroatoms may lead to partial collapses of carbon skeleton and thus decayed cycle stability of the electrode [27]. Hence, an effective approach of synthesizing heteroatom-doped carbons should be

* Corresponding author.
** Corresponding author at: Shanghai Key Lab of Chemical Assessment and Sustainability, School of Chemical Science and Engineering, Tongji University, Shanghai, 200092, China.
E-mail addresses: liumx@tongji.edu.cn (M. Liu), ganlh@tongji.edu.cn (L. Gan).
[1] These authors contributed equally to this work.

https://doi.org/10.1016/j.cclet.2020.02.026
1001-8417/

conceived to maximize the electrostatic interaction and redox reactions.

In this work, we report a straightforward approach to construct N, O-doped carbons ($NOC_{x,y}$, where x reflects the pyrolysis temperature and y demonstrates the *o*-tolidine/*p*-benzoquinone molar ratio) composed of the vast adsorbing surface and diverse faradaic-active species. The present synthetic process allows the transfer of parent heteroatom-containing functionalities to the final carbons. The NOCs have a high adsorption surface (1799 m^2/g), a multi-level micro–meso–macro porous architecture and abundant N/O functionalities, which lower the contact resistance and additionally impart large pseudocapacitive contribution to the total capacitance (311 F/g). Furthermore, the NOC-assembled two-electrode cell affords high faradaic activity in a redox-active solution and yields a high aqueous energy delivery of 18.0 Wh/kg under the power output of 350 W/kg. By utilizing high-voltage electrolytes, the assembled devices display the high energy density up to 74.9 Wh/kg and long cycling lifetime (87.8% retention after 10,000 cycles).

The functional groups of *o*-tolidine/*p*-benzoquinone polymers (PTB_y) are confirmed *via* the Fourier-transformed infrared (FT-IR) spectra in Fig. S1a (Supporting information). Obvious absorptions at 806, 1281, 1488 and 1562 cm^{-1} represent N—H, C—N, C=C and C=O groups [16,28]. X-ray diffraction (XRD) patterns of NOCs (Fig. S1b in Supporting information) show dual broad diffraction peaks at $2\theta = 26°$ and 43°, corresponding to the (002) and (100) diffractions of the amorphous carbonaceous phase [29,30]. The energy dispersive spectroscopy (EDS) mappings depicted in Fig. S1c (Supporting information) present the homogenous distribution of C, N and O elements within NOCs, demonstrating a successful doping of faradaic-active sites. The thermogravimetric analysis indicates the high carbon yields (48%–64%) of PTBs (Fig. S1d in Supporting information). Owing to the electron-donor effect of the primary diamine (*o*-tolidine) and the electron-withdrawing capability of the carbonyl groups (*p*-benzoquinone), *o*-tolidine and *p*-benzoquinone polymerize through Michael addition with amino groups connected at the 2,5-position of *p*-benzoquinone [31]. During the pyrolysis process, benzenoid rings in the polymer serve as cross-linking moieties to join in the carbon skeleton, while N/O faradaic-active sites supplied by the *o*-tolidine/*p*-benzoquinone are gradually anchored into the final matrix.

The wide-scan X-ray photoelectron spectra (XPS) of NOCs (Figs. S2a and b in Supporting information) illustrate the typical N 1s, O 1s and C 1s peaks. As shown in Table S1 (Supporting information), with the rising dosage of N source (*o*-tolidine), the contents of N atom in NOCs go up from 2.56 at% to 4.35 at% and O atom range from 6.59 at% to 8.54 at%. Meanwhile, higher temperature leads to the decreasing of N/O contents from 4.59/12.20 at% to 1.99/5.76 at%. The N 1s spectra shown in Figs. S3a–c (Supporting information) are fitted into four peaks including N-6 (pyridinic N, 398.2 eV), N-5 (pyrrolic N, 399.5 eV), N–Q (quaternary N, 400.3 eV) and N–X (oxidized N, 401.6 eV), respectively [32,33]. By deconvoluting the O 1s spectra, three forms of O element corresponding to O-I (quinone O, 530.7 eV), O-II (C—OH, 532.4 eV) and O-III (O=C—O, 533.6 eV) can be recognized in Figs. S3d–f (Supporting information) [9]. The C 1s spectra (Figs. S3g–i in Supporting information) can be deconvoluted into three types: C—C (284.3 eV), C—N/C—O (285.6 eV) and C=O (287.3 eV), revealing binding situations with N/O species [25]. N/O dopants can break the electroneutrality of neighbored C atoms for a polarized NOC surface, and thus boost the electrode wettability with smaller contact angles (31°–59°) proven in Fig. S4 (Supporting information) [22,23]. Besides, faradaic-active species (N-6, N-5 and O-I) in both N and O atoms could serve as Lewis base sites in acid electrolyte, and provide pseudocapacitance superiority to the ultimate performance [4,34]. As shown in Table S2 (Supporting information), regulating molar ratios in the synthesis leads to a flexible content (2.39%–3.88%) of faradaic-active N and O species. Therefore, the *o*-tolidine/*p*-benzoquinone molar ratio is significant for adjusting the electrode wettability and faradaic activity for high capacitive performance.

Texture parameters of NOCs are investigated by N_2 sorption measurements. The trait of I-type curves (Fig. 1a) in all the NOCs is confirmed by steep uptake of nitrogen ($P/P_0 < 0.05$), manifesting copious micropores [35,36]. The ascending *o*-tolidine interspersed in PTBs makes the polymer skeleton fragile and unable to withstand the high-temperature pyrolysis, and the surface area of $NOC_{700,y}$ gradually declines from 1836 m^2/g to 1454 m^2/g (Table S3 in Supporting information). Besides, a hierarchical architecture in $NOC_{700,1:1}$ (Fig. 1b, insert) is advantageous for continuously offering ion-transfer channels, and thus the effect of pyrolysis temperatures is subsequently investigated. As the temperature elevates from 600 °C to 700 °C, the micropores at 0.5 nm partially develop into abundant larger ones (Fig. 1b) with boosted surface area from 1129 m^2/g to 1799 m^2/g (Table S3). This is because more molecules escape from the carbon matrix during the assisted KOH-activation process. However, excessive pyrolysis temperature (800 °C) leads to the reduction in micropores centered at 0.5 and 0.8 nm (Fig. 1b) and the decrease of surface area (1128 m^2/g, Table S3). The fillings of mesopores in $NOC_{x,1:1}$ are confirmed by small hysteresis loops ($P/P_0 > 0.45$) in Fig. 1a [37]. The tendency of mesoporous distribution evolves from the immature texture ($NOC_{600,1:1}$) to a developed one ($NOC_{700,1:1}$) with more

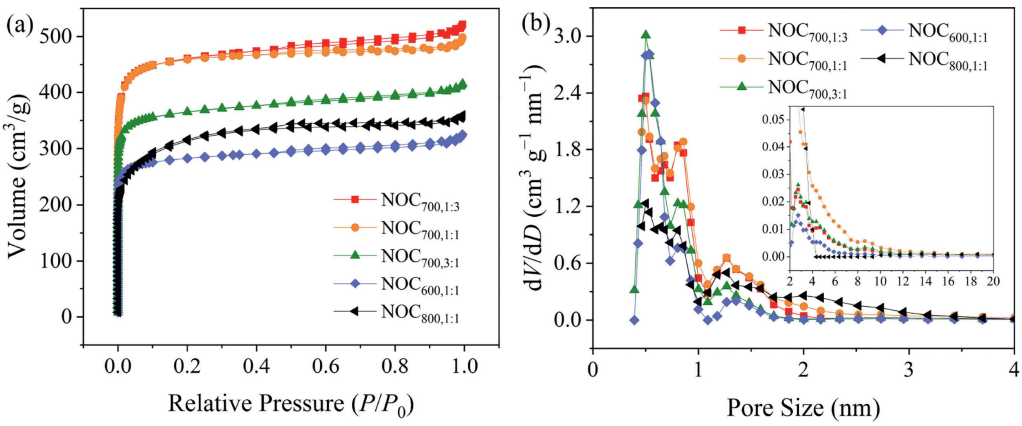

Fig. 1. N_2 sorption isotherms (a) and pore distributions of NOCs (b).

mesopores spreading within 2–10 nm (Fig. 1b, insert) due to the extension/amalgamation of smaller pores with the elevation of heat-treatment temperature [38]. Further increase of temperature results in partial collapses of the carbon framework, and thus leads to the decreased surface area/pore volume for $NOC_{800,1:1}$ (Table S3). The macroporosities of NOCs are proven by scanning electron microscope (SEM). The morphologies presented in Figs. S5a–c (Supporting information) indicate the framework of NOCs become more fragile with the rising dosage of N source (*o*-tolidine). More macropores are observed in $NOC_{700,1:1}$ than in $NOC_{600,1:1}$ in Figs. S5b and d (Supporting information). Nevertheless, the morphology suffers from structural fracture owing to excessive pyrolysis at 800 °C (Fig. S5e in Supporting information). Therefore, optimized molar ratio and pyrolysis temperature would yield adequate surface area and desirable hierarchically coexisting micro–meso–macro structures for double interlayer adsorption and ion diffusion.

Electrochemical performances of NOCs are first investigated in a three-electrode configuration. Compared with the nearly rectangular cyclic voltammetry (CV) curves and isosceles-triangular shaped galvanostatic charging/discharging (GCD) profiles in the KOH electrolyte (Figs. S6a and b in Supporting information), the extra redox peaks illustrated in Fig. 2a and slight distortions in Fig. 2b verify the occurrence of faradaic reactions by N, O-containing functionalities (N-6, N-5 and O-I) gaining/losing protons in an acidic solution (Fig. S6c in Supporting information) [39–41]. The gravimetric capacitances calculated by the GCD discharging branches are 232/251 ($NOC_{700,1:3}$), 290/311 ($NOC_{700,1:1}$), 212/232 ($NOC_{700,3:1}$), 251/272 ($NOC_{600,1:1}$), 209/237 F/g ($NOC_{800,1:1}$) in KOH/H_2SO_4 electrolytes, respectively. The optimal $NOC_{700,1:1}$ electrode also gives strong rate capability (Figs. S6d and e in Supporting information) with capacitance retention of 66% in KOH and 69% in H_2SO_4 at 10 A/g. It can be found that as the pyrolysis temperature rises from 600 °C to 700 °C, the capacitances exhibit an obvious improvement (Fig. 2b). This is mainly because sufficient pyrolysis at 700 °C guarantees a developed porous architecture equipped with better conductivity and lower contact resistance, which can be validated by electrochemical impedance spectrogram (EIS) plots (Fig. S6f in Supporting information). The ohmic resistance (R_s) deduced by the first Z' intersection is only 0.25 Ω for $NOC_{700,1:1}$, suggesting that the electrode possesses a low internal/contact resistance [42]. Moreover, the small charge-transfer resistance (R_{ct}) value (0.84 Ω) and the Warburg impedance (W, 0.45 Ω) can guarantee the superb propagation capability for ions within $NOC_{700,1:1}$ [43]. Further increase of pyrolysis temperature to 800 °C brings about decayed utilization of adsorbing surface, which explains the unsatisfactory capacitance of $NOC_{800,1:1}$ in Fig. 2b. Meanwhile, faradaic-active species regulated by *o*-tolidine/*p*-benzoquinone molar ratios endow the electron-donor features and supply abundant electrochemically active sites. To better confirm the pseudocapacitive contributions, the relationship between specific capacitance and square root of charge/discharge time is plotted in Fig. S6g (Supporting information). The Y-intercepts account for the rate-independent parts, while the remainders of total capacitances are pseudocapacitances [44]. The correlation between capacitances, surface areas and faradaic-active heteroatom species is given in Fig. 2c. With the increasing faradaic-active heteroatom species, the pseudocapacitive contribution is evidenced by a scrambling tendency from 35% to 39%. However, excessive introduction of N-containing dopants leads to a decayed surface area of the flimsy carbon matrix for physical adsorption, and renders $NOC_{700,3:1}$ with inferior capacitive performance. Therefore, $NOC_{700,1:1}$ takes full use of the integrated superiorities from adsorbing surface and faradaic-active sites, obtaining a maximized capacitance.

Regarding practical applications, $NOC_{700,1:1}$ electrodes are assembled into a symmetric cell with the redox-active hybrid electrolyte H_2SO_4+KI. The larger CV integral area in H_2SO_4+KI (Fig. 3a) originates from the four additional redox couples ($3I^-/I_3^-$, $2I^-/I_2$, $2I_3^-/3I_2$ and $I_2/2IO_3^-$). The reversible reactions between them contribute to the extra paired redox peaks providing additional pseudocapacitance [45–47]. Additionally, the similar standard potential of redox couples causes O_2 evolution potential shift, hindering H_2O electrolysis and enlarging the device potential from 1.2 V to 1.4 V [45,48]. The CV curves display highly symmetric rectangular profiles and maintain nearly rectangle even at 100 mV/s (Fig. S7a in Supporting information) due to the outstanding ion sorption reversibility [49]. As exhibited in GCD profiles (Fig. 3b), the capacitance performance of $NOC_{700,1:1}$ reaches a higher level of 264 F/g @ 0.5 A/g in H_2SO_4 + KI which is 1.18-fold reinforcement than in H_2SO_4 (228 F/g). The small R_{ct} and R_s values (1.91 and 0.47 Ω for H_2SO_4+KI cell, and 1.46 and 0.19 Ω for H_2SO_4 one) indicate low internal resistances (Fig. S7b in Supporting information). High-energy storage is achieved benefited from the double-win of enlarged voltage window (1.2 V–1.4 V) and enhanced capacitance generated by redox-active electrolyte. The faradaic-active cell exhibits energy exports of 18.0 Wh/kg at the power source of 350 W/kg and maintains 13.8 Wh/kg @ 7000 W/kg in H_2SO_4 + KI, enhancing greatly compared with the energy/power properties in H_2SO_4 (11.4 Wh/kg @ 300 W/kg and 8.0 Wh/kg @ 6000 W/kg, Fig. 3c). Besides, the device shows an outstanding electrochemical life over a consecutive charging-discharging process. Notably, considerable capacitance enhancement by the enlarged faradic effect renders the performance higher in H_2SO_4 + KI (199 F/g) than in H_2SO_4 (188 F/g) even after 10,000 cycles (Fig. S7c in Supporting information). Therefore, N, O-containing species furnish faradaic-active sites to react with redox pairs in H_2SO_4 + KI, thus feasible for energy storage in terms of both the device potential and pseudocapacitive activity.

Due to the enhanced electrochemical behavior caused by a superior ion-accessible platform and an ideal nanoarchitecture, the $NOC_{700,1:1}$ electrodes are subsequently fabricated into symmetric cells using 1 mol/L Na_2SO_4, 7 mol/kg Li-TFSI and $EMIMBF_4$. The quasi-rectangular/triangular shaped CV/GCD

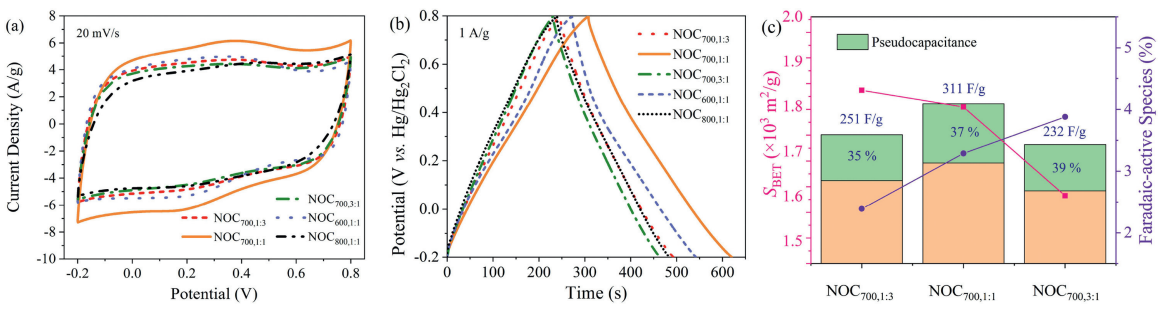

Fig. 2. CV/GCD curves (a, b) of NOCs in 1 mol/L H_2SO_4. The relationships between capacitances and surface area/faradaic-active species (c).

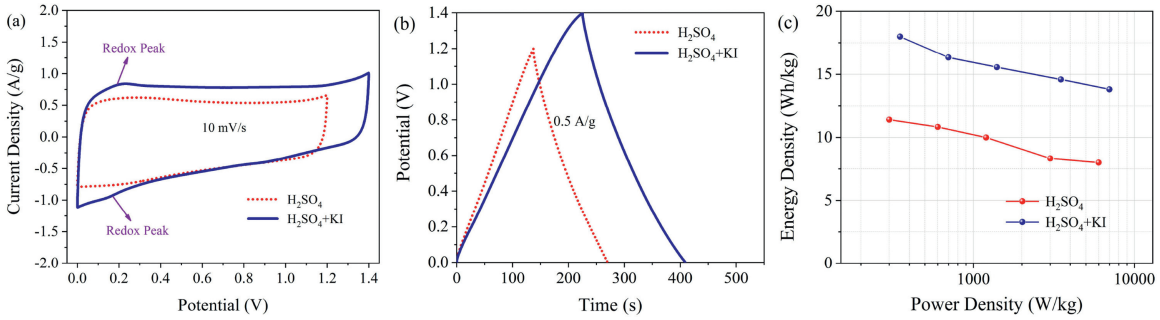

Fig. 3. Comparison of CV/GCD curves ($NOC_{700,1:1}$) in a two-electrode H_2SO_4 + KI device with H_2SO_4 electrolyte (a, b) and Ragone plots (c).

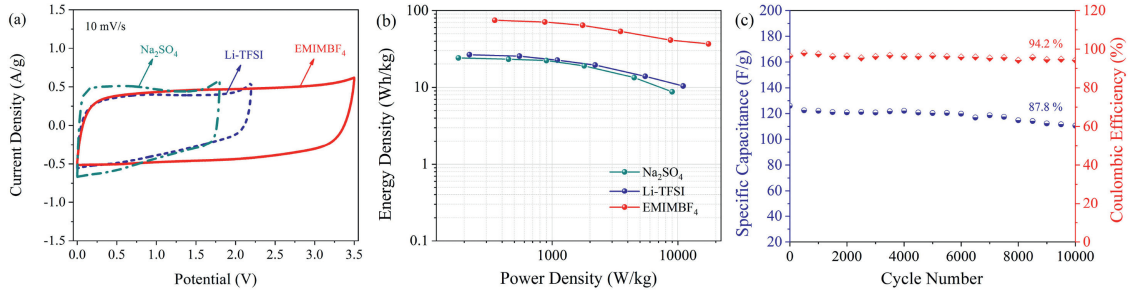

Fig. 4. Two-electrode electrochemical tests of $NOC_{700,1:1}$ using 1 mol/L Na_2SO_4, 7 mol/kg Li-TFSI and $EMIMBF_4$: Comparison of CV curves (a), Ragone plots (b), pattern of Coulombic efficiency and cycling test at 2 A/g in $EMIMBF_4$ (c).

profiles (Fig. 4a and Figs. S8a–c in Supporting information) illustrate high efficiency in the reversible charge-storage process [50]. Compared with Na_2SO_4-loaded symmetric device, the Li-TFSI and $EMIMBF_4$ assembled capacitors show higher R_{ct} values disclosed in Fig. S8d (Supporting information) owing to larger ionic sizes ($TFSI^-$: 0.79 nm, $EMIM^+$: 0.76 nm, BF_4^-: 0.48 nm) [51]. The assembled Na_2SO_4/Li-TFSI/$EMIMBF_4$ cells with significantly broadened potentials offer boosted energy outputs of 24.1/26.5/74.9 Wh/kg (Fig. 4b). Besides, over 10,000 cycles at 2 A/g, the capacitance in $EMIMBF_4$ only decays by 12.2% with 94.2% Coulombic efficiency retaining (Fig. 4c). The NOC-based devices achieve distinguished energy deliveries (Table S4 in Supporting information), advantageous power outputs and prominent cycle stabilities for advanced supercapacitors. Firstly, a high adsorbing surface (1799 m^2/g) promotes physical charge accumulation [17,18]. Secondly, the hierarchical porous texture leads to effective utilization of the carbon surface, in favor of ion-adsorption on the electrode material [11,52]. Thirdly, by doping N/O into carbon matrix, the surface polarization/affinity toward electrolyte can be modified for enhanced electrostatic interaction and fast ion transfer at high rates [22,53]. Besides, the faradaic-active functionalities stem from heteroatoms also yield pseudocapacitive contributions [25].

To conclude, the *in-situ* polymerization/pyrolysis approach is employed to efficiently construct highly active N, O-doped carbons (NOCs), which offers diversified electrochemically active sites, a vast surface area and hierarchical porous texture. A variety of faradaic-active species (N-6, N-5 and O-I) are homogeneously distributed on NOC architecture. Besides, the high adsorption platform (1799 m^2/g) and multi-level channels are optimized for electrostatic accumulation and continuous ion-transmission. Consequently, a 37% pseudocapacitive contribution and a corresponding maximized capacitance (311 F/g) are obtained by the as-prepared NOC electrode. A reinforced energy delivery (18.0 Wh/kg) at a higher power output (350 W/kg) is achieved *via* the electron gaining/losing process of the redox-pairs in the aqueous faradaic-active cell. The $NOC_{700,1:1}$-assembled capacitor also possesses a competitive energy density (74.9 Wh/kg) and high-potential stability (87.8% retention after 10,000 cycles) in $EMIMBF_4$. We believe this *in-situ* polymerization/pyrolysis approach will open up an avenue toward ameliorating both faradaic activity and nano-architecture for promising energy-storage apparatuses.

Declaration of competing interest

The authors declare that they have no known competing financial interests or personal relationships that could have appeared to influence the work reported in this paper.

Acknowledgments

This work was financially supported by the National Natural Science Foundation of China (Nos. 21905207, 21875165, 51772216, and 21703161), the Science and Technology Commission of Shanghai Municipality, China (No. 14DZ2261100), and the Natural Foundation of Hubei Province of China (No. 2014CFB782) and the Fundamental Research Funds for the Central Universities.

Appendix A. Supplementary data

Supplementary material related to this article can be found, in the online version, at doi:https://doi.org/10.1016/j.cclet.2020.02.026.

References

[1] S. Choudhury, S. Stalin, D. Vu, et al., Nat. Commun. 10 (2019) 4398.
[2] H.G. Jung, J. Hassoun, J.B. Park, et al., Nat. Chem. 4 (2012) 579–585.
[3] F. Wang, X. Wu, X. Yuan, et al., Chem. Soc. Rev. 46 (2017) 6816–6854.
[4] W. Zhang, C. Xu, C. Ma, et al., Adv. Mater. 29 (2017) 1701677.
[5] C. Peng, J. Yu, S. Chen, L. Wang, Chin. Chem. Lett. 30 (2019) 1137–1140.
[6] S. Witomska, Z. Liu, W. Czepa, et al., J. Am. Chem. Soc. 141 (2019) 482–487.
[7] F. Wei, X. He, H. Zhang, et al., J. Power Sources 428 (2019) 8–12.
[8] A. González, E. Goikolea, J.A. Barrena, R. Mysyk, Renew. Sustain. Energy Rev. 58 (2016) 1189–1206.

[9] Y. Liao, H. Wang, M. Zhu, A. Thomas, Adv. Mater. 30 (2018) 1705710.
[10] C. Wang, D. Wu, H. Wang, et al., J. Mater. Chem. A 6 (2018) 1244–1254.
[11] H. Zhong, F. Xu, Z. Li, et al., Nanoscale 5 (2013) 4678–4682.
[12] S.K. Das, K. Bhunia, A. Mallick, et al., Microporous Mesoporous Mater. 266 (2018) 109–116.
[13] B. You, L. Wang, L. Yao, J. Yang, Chem. Commun. 49 (2013) 5016–5018.
[14] J. Zhu, Y. Dong, S. Zhang, Z. Fan, Acta Phys. -Chim. Sin. 36 (2020) 1903052.
[15] S.S. Karade, B.R. Sankapal, ACS Sustain. Chem. Eng. 6 (2018) 15072–15082.
[16] M.P. Chavhan, S. Ganguly, Carbon 154 (2019) 33–41.
[17] J. Zhao, H. Lai, Z. Lyu, et al., Adv. Mater. 27 (2015) 3541–3545.
[18] D. Xue, D. Zhu, H. Duan, et al., Chem. Commun. 55 (2019) 11219–11222.
[19] N. Fu, J. Yu, J. Zhao, et al., Carbon 149 (2019) 538–545.
[20] W. Lei, J. Guo, Z. Wu, et al., Sci. Bull. 62 (2017) 1011–1017.
[21] Y. Lu, J. Liang, S. Deng, et al., Nano Energy 65 (2019) 103993.
[22] P. Sazama, J. Pastvova, C. Rizescu, et al., ACS Catal. 8 (2018) 1779–1789.
[23] H. Zhou, Y. Zhou, L. Li, et al., ACS Sustain. Chem. Eng. 7 (2019) 9281–9290.
[24] L. Sun, H. Zhou, L. Li, et al., ACS Appl. Mater. Interfaces 9 (2017) 26088–26095.
[25] L. Miao, H. Duan, Z. Wang, et al., Chem. Eng. J. 382 (2020) 122945.
[26] M. Zhang, C. Yu, Z. Ling, et al., Green Chem. 21 (2019) 2095–2103.
[27] W.J. Lee, J. Lim, S.O. Kim, Small Methods 1 (2017) 1600014.
[28] R. Rajak, M. Saraf, S.M. Mobin, J. Mater, Chem. A 7 (2019) 1725–1736.
[29] L. Miao, X. Qian, D. Zhu, et al., Chin. Chem. Lett. 30 (2019) 1445–1449.
[30] W. Li, B. Li, M. Shen, et al., Chem. Eng. J. 384 (2020) 123309.
[31] B.D. Mather, K. Viswanathan, K.M. Miller, T.E. Long, Prog. Polym. Sci. 31 (2006) 487–531.
[32] Z. Song, H. Duan, D. Zhu, et al., J. Mater. Chem. A 7 (2019) 15801–15811.
[33] L. Li, Y. Zhou, H. Zhou, et al., ACS Sustain. Chem. Eng. 7 (2018) 1337–1346.
[34] Y. Dong, W. Wang, H. Quan, et al., ChemElectroChem 3 (2016) 814–821.
[35] J. Yan, D. Zhu, Y. Lv, et al., Chin. Chem. Lett. 31 (2020) 579–582.
[36] F. Wei, H. Bi, S. Jiao, X. He, Acta Phys. -Chim. Sin. 36 (2020) 1903043.
[37] Y. Li, G. Wang, T. Wei, et al., Nano Energy 19 (2016) 165–175.
[38] Y. Liu, J. Cao, X. Jiang, et al., J. Mater. Chem. A 6 (2018) 6891–6903.
[39] X. Yu, C. Pei, L. Feng, Chin. Chem. Lett. 30 (2019) 1121–1125.
[40] H. Li, J. Li, A. Thomas, Y. Liao, Adv. Funct. Mater. 29 (2019) 1904785.
[41] H.A. Andreas, B.E. Conway, Electrochim. Acta 51 (2006) 6510–6520.
[42] F. Sun, Z. Qu, J. Gao, et al., Adv. Funct. Mater. 28 (2018) 1804190.
[43] J. Yu, C. Yu, W. Guo, et al., Nano Energy 64 (2019) 103921.
[44] J.S.M. Lee, M.E. Briggs, C.C. Hu, A.I. Cooper, Nano Energy 46 (2018) 277–289.
[45] B. Nagar, D.P. Dubal, L. Pires, et al., ChemSusChem 11 (2018) 1849–1856.
[46] C. Zhong, Y. Deng, W. Hu, et al., Chem. Soc. Rev. 44 (2015) 7484–7539.
[47] K. Jayaramulu, D.P. Dubal, B. Nagar, et al., Adv. Mater. 30 (2018) 1705789.
[48] S.J. Yoo, B. Evanko, X. Wang, et al., J. Am. Chem. Soc. 139 (2017) 9985–9993.
[49] C. Chen, G. Xu, X. Wei, L. Yang, J. Mater. Chem. A 4 (2016) 9900–9909.
[50] L. Sun, Y. Zhou, L. Li, et al., Appl. Surf. Sci. 467 (2019) 382–390.
[51] P. Simon, Y. Gogotsi, Nat. Mater. 7 (2008) 845–854.
[52] M. Fu, W. Chen, X. Zhu, et al., Carbon 141 (2019) 748–757.
[53] X. Qian, L. Miao, J. Jiang, et al., Chem. Eng. J. 388 (2020) 124208.